iScience

CellPress
OPEN ACCESS

Article

Comparison of applied torque and energy conversion efficiency between rotational triboelectric nanogenerator and electromagnetic generator

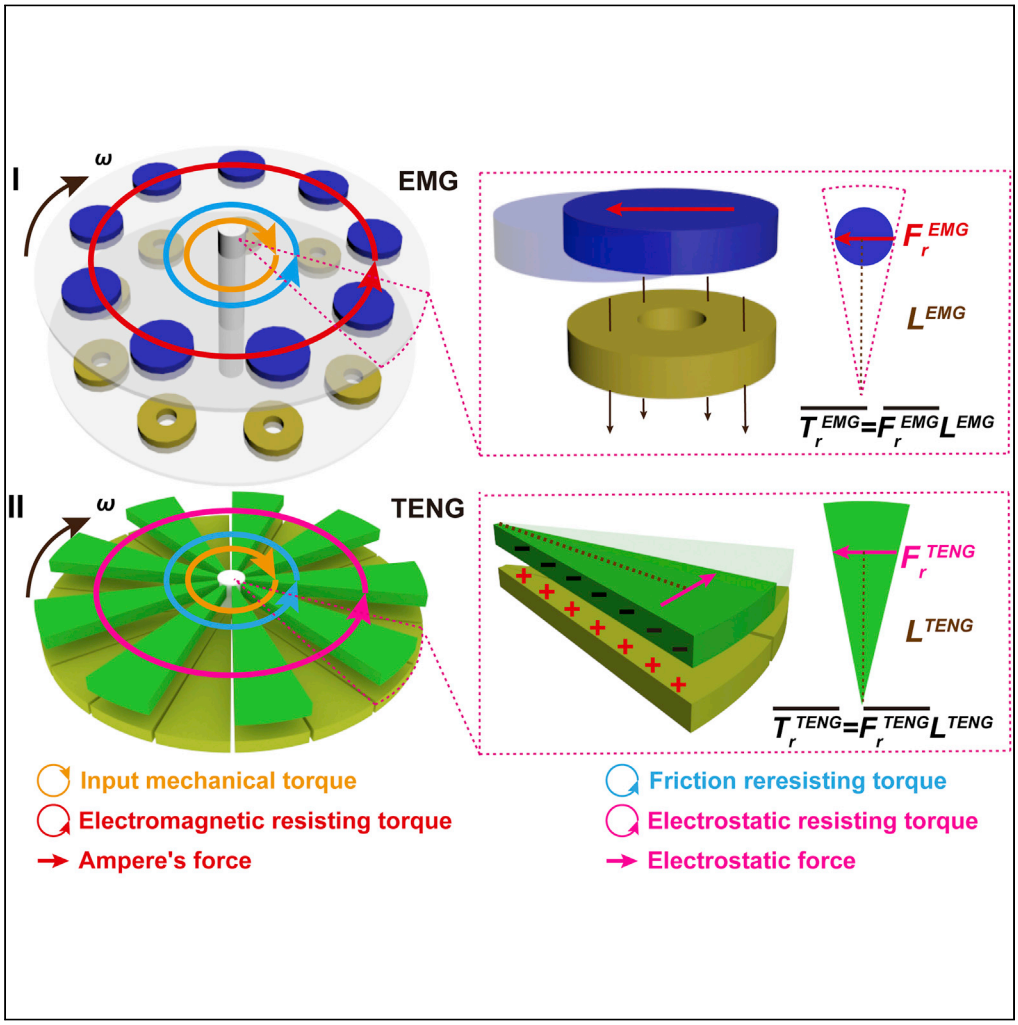

Shaohang Xu, Xianpeng Fu, Guoxu Liu, Tong Tong, Tianzhao Bu, Zhong Lin Wang, Chi Zhang

czhang@binn.cas.cn

Highlights

The applied torque of the rotating EMG and TENG are systematically measured

The energy conversion efficiencies of both generators are quantified and compared

This work has demonstrated a remarkable merit of the TENG under a gentle-triggering

Xu et al., iScience *24*, 102318
April 23, 2021
https://doi.org/10.1016/j.isci.2021.102318

iScience

CellPress
OPEN ACCESS

Article

Comparison of applied torque and energy conversion efficiency between rotational triboelectric nanogenerator and electromagnetic generator

Shaohang Xu,[1,2,5] Xianpeng Fu,[1,2,5] Guoxu Liu,[1,2] Tong Tong,[1,2] Tianzhao Bu,[1,2] Zhong Lin Wang,[1,2,3] and Chi Zhang[1,2,4,6,*]

SUMMARY

Triboelectric nanogenerator (TENG) is regarded as an equally important mechanical energy harvesting technology as electromagnetic generator (EMG). Here, the input mechanical torques and energy conversion efficiencies of the rotating EMG and TENG are systematically measured, respectively. At constant rotation rates, the input mechanical torque of EMG is balanced by the friction resisting torque and electromagnetic resisting torque, which increases with the increasing rotation rate due to Ampere force. While the input mechanical torque of TENG is balanced by the friction resisting torque and electrostatic resisting torque, which is nearly constant at different rotation rates. The energy conversion efficiency of EMG increases with the increasing input mechanical power, while that of the TENG remains nearly constant. Compared with the EMG, the TENG has a higher conversion efficiency at a low input mechanical power, which demonstrates a remarkable merit of the TENG for efficiently harvesting weak ambient mechanical energy.

INTRODUCTION

With the rapid development of the Internet of Things (Borgia, 2014; Roman et al., 2013), sustainable and long-life energy supply for billions of distributed electronics has become a major issue(Chu and Majumdar, 2012; Gielen et al., 2016). Compared with the traditional energy supply by using chemical battery, energy harvesting technology is a more effective way by converting ambient mechanical energy into electric power (Gao et al., 2020; Guo et al., 2016; Shao et al., 2018b; Xie et al., 2014; Xu et al., 2019). Nowadays, triboelectric nanogenerator (TENG) has attracted growing attention due to its simple structure(Wang et al., 2014; Ye et al., 2019; Zhang et al., 2019a, 2019b), high power density, low cost, high flexibility (Liu et al., 2020; Wang et al., 2020a), and abundant selection of materials (Li et al., 2020; Wang et al., 2020b; Yan et al., 2020; Zheng et al., 2020). Derived from the second term in Maxwell's displacement current (Akande and Lowell, 1985; Wang, 2017), the TENG has been widely used in micro/nanopower sources (Seung et al., 2015; Tayyab et al., 2020; Xiong et al., 2019), self-powered sensing (Jin et al., 2017; Khan et al., 2017; Wu et al., 2016), blue energy (Shao et al., 2018a; Wang et al., 2016), and high voltage sources (Bui et al., 2019; Li et al., 2017; Xia et al., 2019) since its first invention in 2012 (Fan et al., 2012).

As a new energy technology, the TENG has an equally vital role in harvesting mechanical energy compare to the traditional electromagnetic generator (EMG). The TENG has demonstrated to be comparable and symmetrical with EMG in working mechanisms, governing equations, and output characteristics (Zhang et al., 2014), which has demonstrated that the TENG could be equivalently important as the EMG for harvesting mechanical energy. Moreover, the reports have demonstrated that the TENG has a better output performance than EMG at low frequency (Zi et al., 2016) and small amplitude (Zhao et al., 2019), which indicates a great advantages and possible killer applications of TENG in micromechanical energy harvesting and sensing. However, the applied force/torque and energy conversion efficiency of both generators have not systematically studied and compared yet, which are directly influenced by their different damping characteristics. So, it is extremely important to reveal the characteristics of applied force/torque for both generators and investigate the energy conversion efficiency dependence on input mechanical power.

Here in this work, the input mechanical torque of the rotating EMG and TENG are systematically measured, respectively. At constant rotation rates, the input mechanical torque of EMG is balanced by the friction

[1]CAS Center for Excellence in Nanoscience, Beijing Key Laboratory of Micro-nano Energy and Sensor, Beijing Institute of Nanoenergy and Nanosystems, Chinese Academy of Sciences, Beijing 101400, China

[2]School of Nanoscience and Technology, University of Chinese Academy of Sciences, Beijing 100049, China

[3]School of Material Science and Engineering, Georgia Institute of Technology, Atlanta, GA 30332, USA

[4]Center on Nanoenergy Research, School of Physical Science and Technology, Guangxi University, Nanning 530004, China

[5]These authors contributed equally

[6]Lead contact

*Correspondence: czhang@binn.cas.cn

https://doi.org/10.1016/j.isci.2021.102318

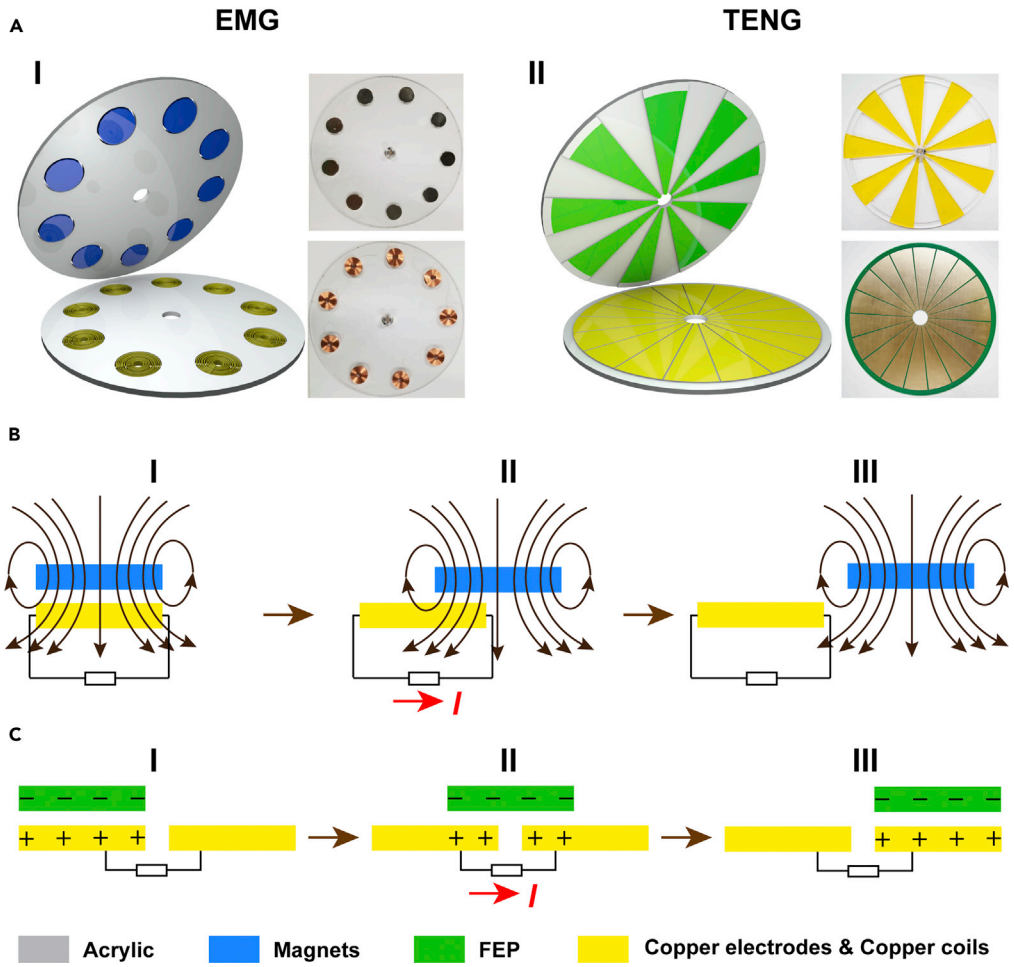

Figure 1. Schematic illustrations and working principles of both fabricated generators

3D schematic diagram and photos of fabricated (A) EMG and TENG. Working principles of (B) EMG and (C) TENG.

resisting torque and electromagnetic resisting torque, which increases with the increasing rotation rate due to Ampere force. While the input mechanical torque of TENG is balanced by the friction resisting torque and electrostatic resisting torque, which is nearly constant at different rotation rates. The energy conversion efficiencies of both generators are also quantified and compared. With the increase of the input mechanical power, the energy conversion efficiency of EMG is increasing, while that of the TENG remains nearly constant. The comparison results and demonstrations have shown that the TENG has a higher conversion efficiency than that of the EMG at a low input mechanical power. This work has demonstrated a remarkable merit of the TENG under a gentle-triggering, which has verified the possible applications for efficiently harvesting weak mechanical energy from human body and ambient environment.

RESULTS

Figure 1 illustrates the schematic diagrams and working principles of the rotational EMG and TENG. Both EMG and TENG contain a rotator and a stator, which are based on the circular acrylic sheets with the same diameter of 280 mm and nine fixed power generation units, as shown in Figure 1A. For the EMG, the magnets and copper coils are embedded in the rotator and stator along the direction of circumference, respectively, as shown in Figure 1A (I). The magnetic poles of the magnet are in the same direction, while the winding direction of the copper coils are all counter clockwise, and the copper coils are connected in parallel. For the TENG, the fan-shaped fluorinated ethylene propylene (FEP) triboelectric layers are adhered to the rotator, while the corresponding fan-shaped copper electrodes are fabricated in the stator as the free-standing mode, which is shown in Figure 1A (II). The detailed fabrication processes of the two generators are described in the Experimental section.

Figure 1B illustrates the working principle of the EMG based on the electromagnetic induction. At the initial state, as shown in Figure 1B (I), the magnets and copper coils are fully aligned. The magnetic flux through the copper coils achieves maximum value. When the magnets rotate away from the copper coils, the magnetic flux through the coil can be changed, which induces an electrodynamic potential and current in the coil, in the state II. The magnetic flux reduces to minimum when the magnets rotate to the final state III. The rotator part rotates continuously to the next initial state that can induce the current flow in the reversed direction. Thus, an alternating current (AC) can be generated for the periodically rotate of these magnets. By coupling of the contact electrification and the relative-sliding-induced charge transfer, the working principle of the freestanding mode TENG is shown in Figure 1C. To generate the equal negative and positive charges on the FEP and copper electrode, the two triboelectric layers are pre-contacted for electrification and then separate in a certain distance. In the process of relative rotation, the small gap is kept between the two triboelectric layers to eliminate the influence of friction. At the original state, the FEP layer is aligned with the left copper electrode. At this state, the TENG is in the electrostatic equilibrium state and no electron flows through the external circuit, as shown in Figure 1C (I). As shown in Figure 1C (II), when the FEP layer rotates under the excitation of input torque, the aligned area between FEP and left electrode is reduced. The produced potential difference will drive electrons to flow from the right to the left electrode. This electricity generation process will last until the FEP rotates to the position where the FEP is aligned with the right copper electrode, as shown in Figure 1C (III). In the following, the aligned area between FEP and left electrode starts to increase, which creates a reverse current. Electrons flow back and forth between the two copper electrodes, generating an AC signal.

For the EMG, according to the Faraday's law, the open-circuit voltage and short-circuit current can be presented as:

$$U_{oc}^{EMG} = -N_1 \frac{d\Phi}{dt} \quad \text{(Equation 1)}$$

$$I_{sc}^{EMG} = \frac{U_{oc}^{EMG}}{r} \quad \text{(Equation 2)}$$

Where N_1 is the number of the coil-magnet pairs and Φ is the total magnetic flux in each coil, r represents the internal resistance of the coil. Apparently, the rate of the magnetic flux variate is related to the rotation rate. Figures 2A and 2C shows the variety of open-circuit voltage and short-circuit current of the EMG at the rotation rate 200 r/min, the open-circuit voltage has the peak to peak values of 16.61V while the short-circuit current has the peak values of 71.48 mA. Considering the Equations (1) and (2), the peak to peak values of open-circuit voltage and the peak values of short-circuit current both increase proportionally with the increases of the rotation rate. The experimental results are given in the illustration of Figures 2A and 2C, respectively, which accord with the theoretical equations. The peak to peak values of open-circuit voltage increases from 0.86 V to 16.61 V, while the peak values of short-circuit current increase from 7.98 mA to 71.48 mA with the rotation rate increases from 10 r/min to 200 r/min.

For the TENG, according to the previous works, the open-circuit voltage and short-circuit current can be described as:

$$U_{oc}^{TENG} = \frac{\sigma S}{C} \quad \text{(Equation 3)}$$

$$I_{sc}^{TENG} = \sigma \frac{\Delta S}{\Delta t} = \sigma \frac{N_2 r^2 \Delta\theta}{2\Delta t} = \frac{N_2}{\pi} \frac{\sigma}{2} S\omega \quad \text{(Equation 4)}$$

where σ is the charge density on the FEP surface, S is the area of one electrode, C is the capacitance between the two electrodes, N_2 is the number of segments of the electrode, ω is the rotational angular velocity ($\omega = \frac{2\pi n}{60}$, where n is the rotation rate). Figures 2B and 2D shows the variety of open-circuit voltage and short-circuit current of the TENG at the rotation rate 200 r/min, the peak to peak values of open-circuit voltage can achieve 1064 V, and the peak values of short-circuit current can achieve 79.01 μA. Considering the Equations (3) and (4), with increasing the rotation rate, the peak values of short-circuit current can increases proportionally while the peak to peak values of open-circuit voltage can almost keep unchanged. As shown in the illustration of Figures 2B and 2D, when the rotation rate increases from 10 r/min to 200 r/min, the peak values of short-circuit current increases from 5.73 μA to 79.01 μA, while the peak values of open-circuit voltage remains almost stable around 1070 V.

For the EMG, the average output power versus external load can be calculated as:

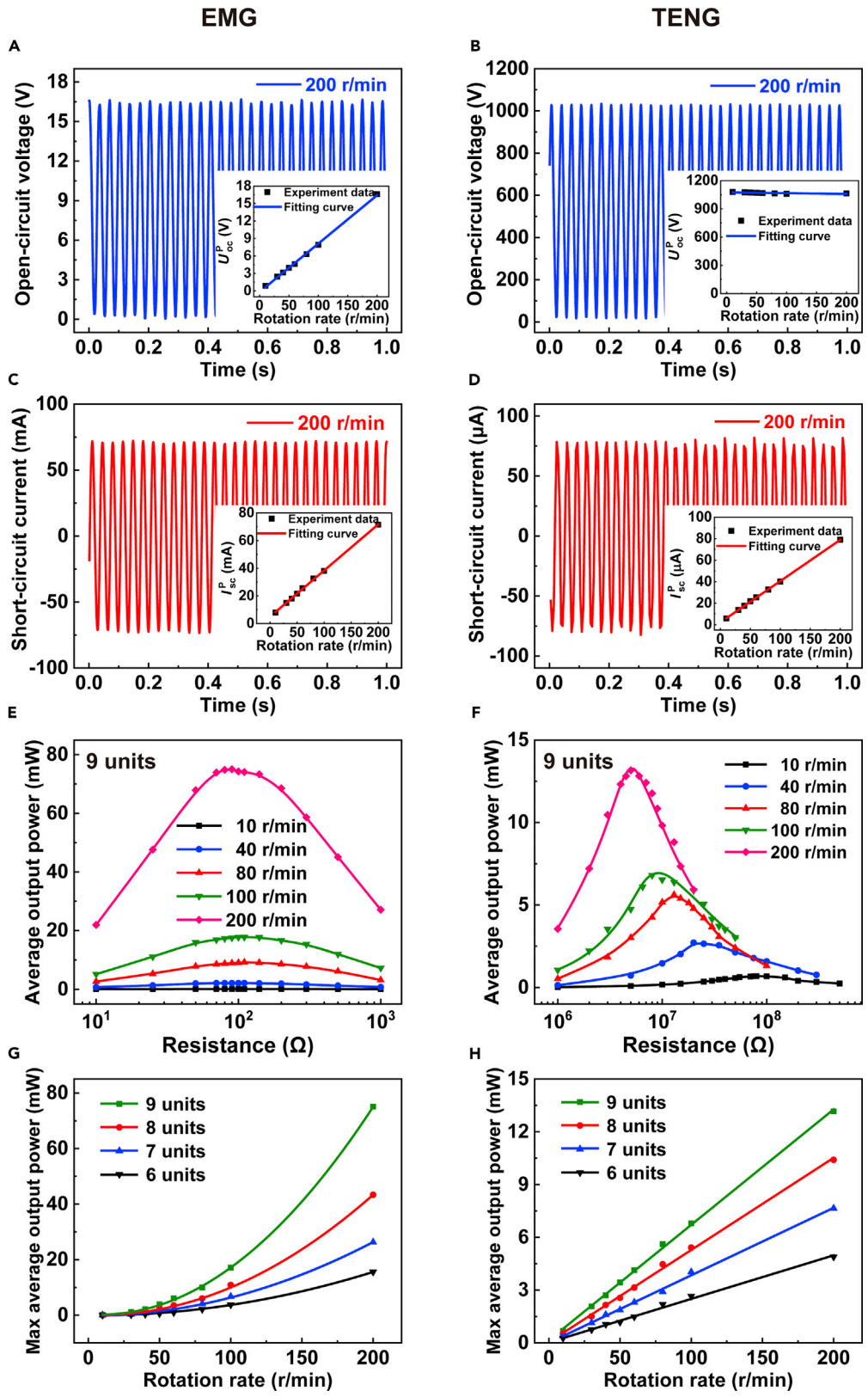
EMG
TENG
A
B
C
D
E
F
G
H
200 r/min
Open-circuit voltage (V)
Time (s)
Experiment data
Fitting curve
Rotation rate (r/min)
Short-circuit current (mA)
Short-circuit current (μA)
9 units
10 r/min
40 r/min
80 r/min
100 r/min
200 r/min
Average output power (mW)
Resistance (Ω)
8 units
7 units
6 units
Max average output power (mW)

Figure 2. The electric output performance comparison of the EMG and TENG

The open-circuit voltages of (A) EMG and (B) TENG with nine power generation units under a rotation rate of 200 r/min, the illustration is the peak to peak values open-circuit voltage of the EMG and TENG with increasing rotation rate from 10 r/min to 200 r/min respectively. The short-circuit currents of (C) EMG and (D) TENG with nine power generation units under a rotation rate of 200 r/min, the illustration is the peak values short-circuit current of the EMG and TENG with increasing rotation rate from 10 r/min to 200 r/min respectively. Impedance matchings of (E) EMG and (F) TENG with nine power generation units and increasing rotation rate from 10 r/min to 200 r/min. The maximum average output powers of (G) EMG and (H) TENG with different number of power generation units and rotation rates.

$$\overline{P_{out}^{EMG}} = \frac{\int_0^{t_1} U_1{}^2 dt}{Rt_1} \quad \text{(Equation 5)}$$

where U_1 is the voltage of the external load, R is the external resistance, t_1 is the integral period. Under the different rotation rate, the average output power of the EMG first increased, and then decreased with increasing the external resistance, the maximum average output power always appears at the external resistance of 110 Ω regardless the rotation rate, which is shown in Figure 2E. Moreover, the average output power of the EMG with different number of power generation units at different rotation rate is shown in Figure S1. And the variety of the maximum average output powers of the EMG with rotation rate at different number of power generation units are summarized in Figure 2G, which are all nearly proportional to the square of the rotation rate.

For the TENG, the average output power versus external load can be calculated as:

$$\overline{P_{out}^{TENG}} = \frac{R\int_0^{t_1} I_1{}^2 dt}{t_1} \quad \text{(Equation 6)}$$

where R is the external resistance, I_1 is the current flowing through the external load, t_1 is the integral period. With increase the external resistance, the variation trend of average output power of the TENG is similar to the EMG. However, the maximum average output power appears at the low external resistance when the rotation rate is high, while the maximum average output power appears at high external resistance when the rotation rate is low, with the increases of the rotation rate from 10 r/min to 200 r/min, the external resistance corresponding to the maximum average output power decreases from 80 MΩ to 5 MΩ, which is shown in Figure 2F. Furthermore, the average output power of the TENG with different number of power generation units at different rotation rate is shown in Figure S1. The variety of the maximum average output powers of the TENG with rotation rate at different number of power generation units are summarized in Figure 2H, which are all nearly proportional to the rotation rate.

As shown in Figure 3A, the input mechanical torque needs to overcome the resisting torques for driving the rotator of the both generators to rotate during the operation. When the rotator rotates with a constant rotation rate, the torques are in equilibrium and can be described as:

$$T_1 = T_2 + T_3 \quad \text{(Equation 7)}$$

where T_1 is the input mechanical torque, T_2 is the field-induced resisting torque, and T_3 is the friction resisting torque from mechanical bearing.

For the EMG, the field-induced resisting torque is the electromagnetic resisting torque which is caused by the ampere's force, as shown in Figure 3A (I). During the rotation, the induced current in the coils will generate an opposite ampere's force with rotating direction for hindering the rotator rotating. Therefore, the average electromagnetic resisting torque can be calculated as:

$$\overline{T_r^{EMG}} = \overline{F_r^{EMG}} L^{EMG} \quad \text{(Equation 8)}$$

where $\overline{F_r^{EMG}}$ is the average ampere's force and L^{EMG} is the equivalent arm of the Ampere's force.

For the TENG, the field-induced resisting torque is the electrostatic resisting torque which is caused by the electrostatic force, as shown in Figure 3A (II). During the rotation, the static charge at the triboelectric films will generate an opposite electrostatic force with rotating direction for hindering the rotator rotating. Therefore, the average electrostatic resisting torque can be calculated as:

$$\overline{T_r^{TENG}} = \overline{F_r^{TENG}} L^{TENG} \quad \text{(Equation 9)}$$

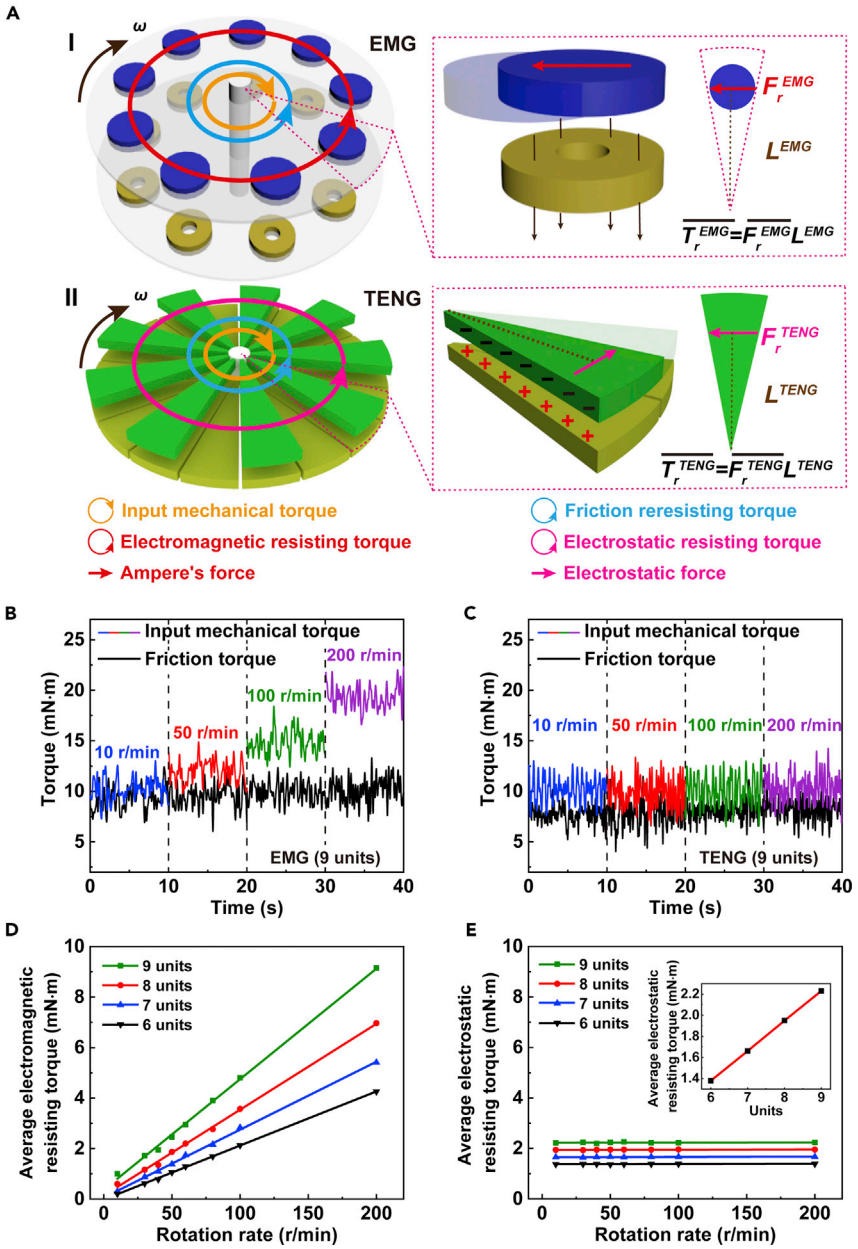

Figure 3. The input mechanical performance comparison of the EMG and TENG

The resisting force and torque analysis of the (A) EMG and TENG. The measured torque of (B) EMG and (C) TENG with different rotation rate. Average field-induced resisting torque of (D) EMG and (E) TENG with different rotation rate.

where $\overline{F_r^{TENG}}$ is the electrostatic force and L^{TENG} is the equivalent arm of the electrostatic force.

As shown in Figure S2, the input mechanical torque of the both generators can be measured by the torque sensor. Firstly, the input mechanical torques are measured at different rotation rates without field-induced resistances ($T_2 = 0$). In these states, the friction resisting torque from mechanical bearing T_3 can be acquired which is just counteracting the measured input mechanical torque T_1, as shown with black curves in Figures 3B and 3C. And then, the input mechanical torques T_1 are measured with field-induced resistances, in the maximum average output power point at different rotation rates, as shown with color curves in Figures 3B and 3C. In addition, the input mechanical torques and friction resisting torque of both generators with different number of power generation units is shown in Figure S3.

For both generators, the acquired friction resisting torque is fluctuating at each rotation rate, but the average value nearly keeps a constant with the increasing of rotation rate. The measured input mechanical torques are also fluctuating. For the EMG, the average value increases with the increasing of rotation rate. It is because that the increasing of rotation rate leads to the increase of induced current and ampere's force. Therefore, the electromagnetic resisting torque increases with the increasing of the rotation rate. While for the TENG, the average value nearly keeps constant with the increasing of rotating rate. It is because that the total amount of tribo-induced electrostatic charges is constant. Therefore, the electrostatic force and resisting torque is not influenced by the rotation rate.

According to Equation (7), the field-induced resisting torque T_2 can be calculated. Figures 3D and 3E summarize the acquired average electromagnetic and electrostatic resisting torques of the EMG and TENG with different number of power generation units versus the rotation rate, respectively. For the EMG, the average electromagnetic resisting torque increases with the increasing rotation rate for each different number of power generation units. Different from the EMG, the average electrostatic resisting torque of the TENG nearly keeps constant with the increasing rotation rate and linearly increases with the unit number, which is shown in the inset of Figure 3E.

The average input mechanical power of the both generators can be described as:

$$\overline{P_{in}} = \overline{T_r} \cdot \omega \qquad \text{(Equation 10)}$$

where $\overline{T_r}$ is the average electromagnetic or electrostatic resisting torque of the both generators and ω is the rotating angular velocity. As shown in Figure 4A, the average input mechanical power of the EMG is nearly proportional to the square of the rotation rate for each different number of power generation units. While the average input power of the TENG is nearly proportional to the rotation rate for each different number of power generation units, as shown in Figure 4B.

The electrical energy conversion efficiency can be expressed as:

$$\eta = \frac{\overline{P_{out}}}{\overline{P_{in}}} \qquad \text{(Equation 11)}$$

Maximum average output power of the EMG and TENG with nine power generation units respectively at the different average input power is indicated in Figure 4C. With the increasing of the average input power, the maximum average output power of the EMG and TENG are both increase, but when the average input power is low, the maximum average output power of the TENG is high than that of the EMG, when the average input power exceeds 11.4 mW, the maximum average output power of the EMG will surpass that of the TENG. Each electrical energy conversion efficiency variation of the both generators versus average input mechanical powers are also shown in Figure 4D. With the increasing of the average input power from 1.05 mW to 18.61 mW, the electrical energy conversion efficiency of EMG rapidly grows and has a tendency to gradually become saturated. While the electrical energy conversion efficiency of the TENG nearly keeps unchanged but decrease slightly, crossing with the curve of EMG at average input power of 11.4 mW. The results indicate that the TENG is superior to the EMG with remarkable merits for harvesting mechanical energy in low input power (<11.4 mW).

For the EMG, the reason for the efficiency characteristic curve which rapidly grows first and then remains virtually constant is that impact by the eddy current loss, copper loss, and other loss. When the average input power is low, the average output power is correspondingly low, the losses occupies a large proportion, which have a greater affection on average output power, and result in the low electrical energy conversion efficiency. With the increasing of the average input power, the average output power increases rapidly, the proportion of losses become lower, and the impact of losses on average output power would reduce and further increase the electrical energy conversion efficiency.

For the TENG, the ideal conversion efficiency can keep constant with the increasing of the average input power; this is because the conversion efficiency of TENG is only related to electrostatic torque which can keep unchanged under different rotation rate. In fact, the conversion efficiency of TENG slightly decreases with the increasing of the average input power. It is because that the slight mechanical vibration will cause the energy loss when the average input power is high.

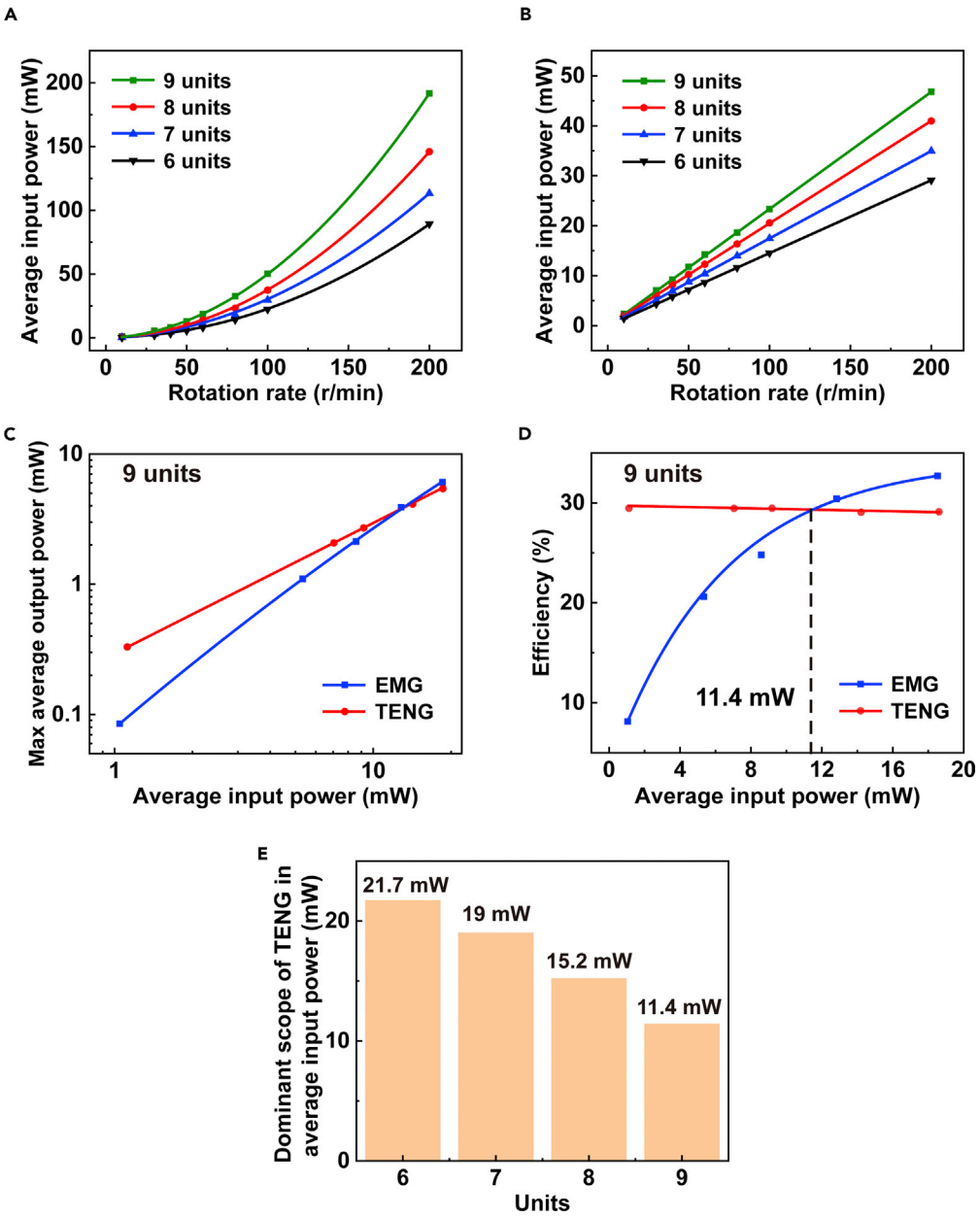

Figure 4. The input power and efficiency comparison of the EMG and TENG

Average input power of (A) EMG and (B) TENG with different rotation rates. Max average output power (C) and energy conversion efficiency (D) comparison of EMG and TENG with different average input power. Dominant scope of TENG in average input power with different number of units (E).

The maximum average output power and electrical energy conversion efficiency of the both generators versus average input power at each different number of power generation units are shown in Figure S4, which all have similar variation tendency. For the eight, seven and six power generation units of both generators, the electrical energy conversion efficiency of EMG increases to the same value as that of the TENG when the average input power increases to 15.2 mW, 19 mW and 21.7 mW, respectively. The average input power at the intersection of electrical conversion efficiency increases with the decreasing unit number, as summarized in Figure 4E. The results show that the fewer the number of power generation units for both generators, the larger dominant power range for the TENG. As the applied torque of the TENG is proportional to the unit number, the results also demonstrate the remarkable merit of TENG in weak input force/torque.

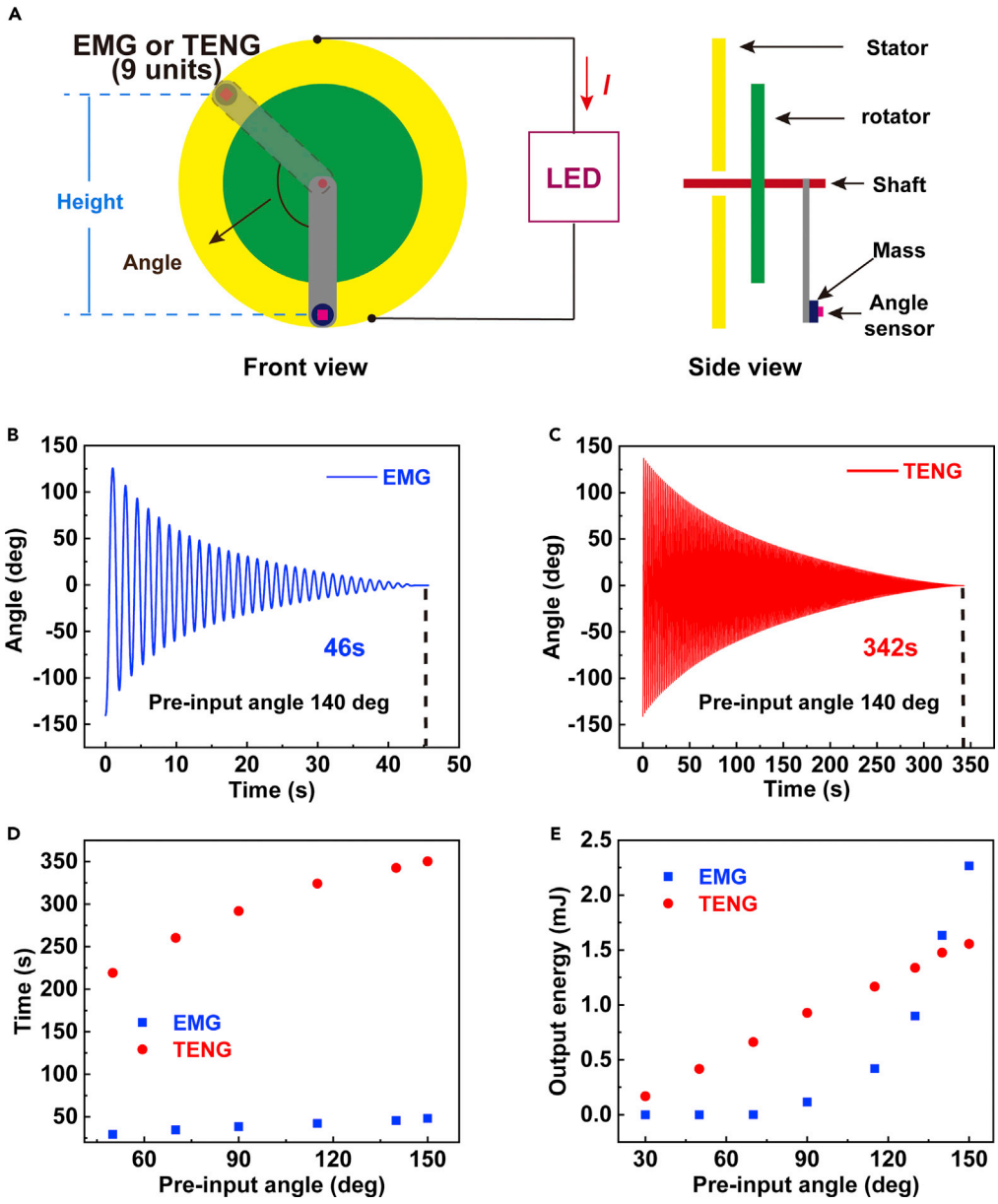

Figure 5. Demonstration for weak mechanical harvesting energy, which EMG and TENG with nine power generation units, respectively

Schematic of the EMG or TENG (A). The variety of swing angle of EMG (B) and TENG (C) at pre-input angle of 140 deg. Swing time of the EMG and TENG versus pre-input angle (D). Output energy of an LED driven by the EMG and TENG versus pre-input angle (E).

We have designed and demonstrated the merit of the TENG for harvesting weak mechanical energy with low input power, as shown in Figure 5A. The EMG and TENG work at the same input mechanical energy which is decided by the gravitational potential energy of the mass and can be tuned by changing the pre-input angle of the mass. An angle sensor is attached to the mass which is used to locate the pre-input angle of the mass and monitor the angle change in real time. The total working time under the same input energy of the both generators are also can achieve. Among them, both EMG and TENG with nine power generation units.

The oscillation curve of the swing angle for the EMG and TENG under pre-input angle 140 deg is shown in Figures 5B and 5C. The swing time of the EMG is 46 s while the TENG is 342 s. The oscillation curve of the

swing angle for the EMG and TENG under pre-input angle 90 and 115 deg is shown in Figure S5. Changing the pre-input angle of the mass, the swing times of EMG and TENG also changes, which are summarized as shown in Figure 5D. The huge difference in the swing time between the both generators indicates that the TENG has much lower damping than the EMG.

Figure 5E shows the output energy of the EMG and TENG across the LED with different pre-input angle, which can be calculated as:

$$E_{out} = \int_0^{t_2} U_2 I_2 dt \qquad \text{(Equation 12)}$$

where t_2 is the swing time, U_2 and I_2 is the voltage and current across the LED applied by the both generators, respectively. The output energy of the TENG across the LED rise slowly, while the EMG rise slowly and then rapidly rise, exceed TENG after 140°. The variation of the U_2 and I_2 at different pre-input angle are shown in Figures S6–S8.

The visual demonstration is shown in Videos S1 and S2. The on/off state of the LED is determined by the input mechanical energy, which is tuned by changing the pre-input angle. When the pre-input angle exceeds 50 deg, the TENG can light up the LED, while the EMG cannot light up until the pre-input angle exceeds 90 deg. As the pre-input angle increases, the brightness of the LED lighted by TENG and EMG both gradually increases. The brightness of LED lighted by the EMG sharply increases and exceeds that of TENG after 115 deg. All these results demonstrate the remarkable merit of the TENG than the EMG in harvesting weak mechanical energy.

DISCUSSION

In summary, this work has investigated the applied torque and energy conversion efficiency of the EMG and TENG, which proves that the TENG has a higher conversion efficiency than that of the EMG at the low input mechanical power. The input mechanical torques of the rotating EMG and TENG are systematically measured, respectively. At constant rotation rates, the input mechanical torque of EMG is balanced by the friction resisting torque and electromagnetic resisting torque, which increases with the increasing rotation rate due to Ampere force. While the input mechanical torque of TENG is balanced by the friction resisting torque and electrostatic resisting torque, which is nearly constant at different rotation rates. The energy conversion efficiencies of both generators are also quantified and compared. With the increase of the input mechanical power, the energy conversion efficiency of EMG is increasing, while that of the TENG remains nearly constant. The comparison results and demonstrations have shown that the TENG has a higher conversion efficiency than that of the EMG at a low input mechanical power. Moreover, the fewer the number of power generation units for both generators, the larger dominant power range for the TENG. In the energy conversion demonstration, an LED powered by the TENG and EMG in the same input mechanical energy has been exhibited. The TENG rather than the EMG can light up the LED by a small mechanical energy. This work has demonstrated a remarkable merit of the TENG under a gentle-triggering, which has verified the possible applications for efficiently harvesting weak mechanical energy from human body and ambient environment.

Limitations of the study

The applied torque, input mechanical power and energy conversion efficiencies of the rotational EMG and TENG are systematically investigated and compared. The results have demonstrated the triboelectric nanogenerator is more suitable for harvesting weak input mechanical energy. However, this method for measuring applied torque, input mechanical power and energy conversion efficiencies is only applicable to the rotational mode. For the TENGs in other modes such as contact-separation mode, further research on measurement methods are expected in the near future.

Resource availability

Lead contact

Further information and requests for resources and reagents should be directed to and will be fulfilled by the lead contact, Chi Zhang.

Materials availability

This study did not generate new unique reagents.

Data and code availability

We do not have any code and upon request we can provide the original data.

METHODS

All methods can be found in the accompanying transparent methods supplemental file.

SUPPLEMENTAL INFORMATION

Supplemental information can be found online at https://doi.org/10.1016/j.isci.2021.102318.

ACKNOWLEDGMENTS

The authors thank the support of the National Natural Science Foundation of China (51922023, 61874011), Beijing Talents Foundation (2017000021223TD04), Tribology Science Fund of State Key Laboratory of Tribology (SKLTKF19B02), and Open Research Foundation of State Key Laboratory of Digital Manufacturing Equipment and Technology (DMETKF2020014).

AUTHOR CONTRIBUTIONS

S.X., X.F., Z.L.W., and C.Z. designed the experiments, analyzed the data, and wrote the paper. G.L., and T.T. carried out the experiments, discussed the results, and performed theoretical calculations. T.B. discussed the results and assisted with experiments.

DECLARATION OF INTERESTS

The authors declare no competing interests.

INCLUSION AND DIVERSITY

We worked to ensure gender balance in the recruitment of human subjects. We worked to ensure sex balance in the selection of non-human subjects. While citing references scientifically relevant for this work, we also actively worked to promote gender balance in our reference list.

Received: January 24, 2021
Revised: February 28, 2021
Accepted: March 11, 2021
Published: April 23, 2021

REFERENCES

Akande, A.R., and Lowell, J. (1985). Contact electrification of polymers by metals. J. Electrostat. *9*, 1445.

Borgia, E. (2014). The internet of things vision: Key features, applications and open issues. Comput. Commun. https://doi.org/10.1016/j.comcom.2014.09.008.

Bui, V.T., Zhou, Q., Kim, J.N., Oh, J.H., Han, K.W., Choi, H.S., Kim, S.W., and Oh, I.K. (2019). Treefrog Toe pad-inspired micropatterning for high-power triboelectric nanogenerator. Adv. Funct. Mater. *29*, 1–10, https://doi.org/10.1002/adfm.201901638.

Chu, S., and Majumdar, A. (2012). Opportunities and challenges for a sustainable energy future. Nature. https://doi.org/10.1038/nature11475.

Fan, F.R., Tian, Z.Q., and Lin Wang, Z. (2012). Flexible triboelectric generator. Nano Energy *1*, 328–334, https://doi.org/10.1016/j.nanoen.2012.01.004.

Gao, Y., Yan, C., Huang, H., Yang, T., Tian, G., Xiong, D., Chen, N., Chu, X., Zhong, S., Deng, W., et al. (2020). Microchannel-confined MXene based flexible piezoresistive multifunctional micro-force sensor. Adv. Funct. Mater. *30*, 1909603, https://doi.org/10.1002/adfm.201909603.

Gielen, D., Boshell, F., and Saygin, D. (2016). Climate and energy challenges for materials science. Nat. Mater. https://doi.org/10.1038/nmat4545.

Guo, H., Wen, Z., Zi, Y., Yeh, M.H., Wang, J., Zhu, L., Hu, C., and Wang, Z.L. (2016). A water-proof triboelectric-electromagnetic hybrid generator for energy harvesting in Harsh environments. Adv. Energy Mater. *6*, 1–7, https://doi.org/10.1002/aenm.201501593.

Jin, L., Deng, W., Su, Y., Xu, Z., Meng, H., Wang, B., Zhang, H., Zhang, B., Zhang, L., Xiao, X., et al. (2017). Self-powered wireless smart sensor based on maglev porous nanogenerator for train monitoring system. Nano Energy *38*, 185–192, https://doi.org/10.1016/j.nanoen.2017.05.018.

Khan, U., Kim, T.H., Ryu, H., Seung, W., and Kim, S.W. (2017). Graphene tribotronics for electronic skin and touch screen applications. Adv. Mater. *29*, 2–8, https://doi.org/10.1002/adma.201603544.

Li, A., Zi, Y., Guo, H., Wang, Z.L., and Fernández, F.M. (2017). Triboelectric nanogenerators for sensitive nano-coulomb molecular mass spectrometry. Nat. Nanotechnol. *12*, 481–487, https://doi.org/10.1038/nnano.2017.17.

Li, Y., Xiong, J., Lv, J., Chen, J., Gao, D., Zhang, X., and Lee, P.S. (2020). Mechanically interlocked stretchable nanofibers for multifunctional wearable triboelectric nanogenerator. Nano Energy *78*, 105358, https://doi.org/10.1016/j.nanoen.2020.105358.

Liu, G., Xu, S., Liu, Y., Gao, Y., Tong, T., Qi, Y., and Zhang, C. (2020). Flexible drug release device powered by triboelectric nanogenerator. Adv. Funct. Mater. *30*, 1909886, https://doi.org/10.1002/adfm.201909886.

Roman, R., Zhou, J., and Lopez, J. (2013). On the features and challenges of security and privacy in distributed internet of things. Comput. Network.

57, 2266–2279, https://doi.org/10.1016/j.comnet.2012.12.018.

Seung, W., Gupta, M.K., Lee, K.Y., Shin, K.S., Lee, J.H., Kim, T.Y., Kim, S., Lin, J., Kim, J.H., and Kim, S.W. (2015). Nanopatterned textile-based wearable triboelectric nanogenerator. ACS Nano *9*, 3501–3509, https://doi.org/10.1021/nn507221f.

Shao, H., Cheng, P., Chen, R., Xie, L., Sun, N., Shen, Q., Chen, X., Zhu, Q., Zhang, Y., Liu, Y., et al. (2018a). Triboelectric–electromagnetic hybrid generator for harvesting blue energy. Nano Micro Lett. *10*, https://doi.org/10.1007/s40820-018-0207-3.

Shao, J., Jiang, T., Tang, W., Xu, L., Kim, T.W., Wu, C., Chen, X., Chen, B., Xiao, T., Bai, Y., and Wang, Z.L. (2018b). Studying about applied force and the output performance of sliding-mode triboelectric nanogenerators. Nano Energy *48*, 292–300, https://doi.org/10.1016/j.nanoen.2018.03.067.

Tayyab, M., Wang, J., Wang, J., Maksutoglu, M., Yu, H., Sun, G., Yildiz, F., Eginligil, M., and Huang, W. (2020). Enhanced output in polyvinylidene fluoride nanofibers based triboelectric nanogenerator by using printer ink as nano-fillers. Nano Energy *77*, 105178, https://doi.org/10.1016/j.nanoen.2020.105178.

Wang, H., Xu, L., Bai, Y., and Wang, Z.L. (2020a). Pumping up the charge density of a triboelectric nanogenerator by charge-shuttling. Nat. Commun. *11*, 4203, https://doi.org/10.1038/s41467-020-17891-1.

Wang, L., Liu, W., Yan, Z., Wang, F., and Wang, X. (2020b). Stretchable and shape-adaptable triboelectric nanogenerator based on biocompatible liquid electrolyte for biomechanical energy harvesting and wearable human–machine interaction. Adv. Funct. Mater. *2007221*, 1–10, https://doi.org/10.1002/adfm.202007221.

Wang, S., Xie, Y., Niu, S., Lin, L., and Wang, Z.L. (2014). Freestanding triboelectric-layer-based nanogenerators for harvesting energy from a moving object or human motion in contact and non-contact modes. Adv. Mater. *26*, 2818–2824, https://doi.org/10.1002/adma.201305303.

Wang, X., Wen, Z., Guo, H., Wu, C., He, X., Lin, L., Cao, X., and Wang, Z.L. (2016). Fully packaged blue energy harvester by hybridizing a rolling triboelectric nanogenerator and an electromagnetic generator. ACS Nano *10*, 11369–11376, https://doi.org/10.1021/acsnano.6b06622.

Wang, Z.L. (2017). On Maxwell's displacement current for energy and sensors: the origin of nanogenerators. Mater. Today *20*, 74–82, https://doi.org/10.1016/j.mattod.2016.12.001.

Wu, J.M., Lin, Y.H., and Yang, B.Z. (2016). Force-pad made from contact-electrification poly(ethylene oxide)/InSb field-effect transistor. Nano Energy *22*, 468–474, https://doi.org/10.1016/j.nanoen.2016.02.048.

Xia, K., Zhu, Z., Fu, J., Li, Y., Chi, Y., Zhang, H., Du, C., and Xu, Z. (2019). A triboelectric nanogenerator based on waste tea leaves and packaging bags for powering electronic office supplies and behavior monitoring. Nano Energy *60*, 61–71, https://doi.org/10.1016/j.nanoen.2019.03.050.

Xie, Y., Wang, S., Niu, S., Lin, L., Jing, Q., Yang, J., Wu, Z., and Wang, Z.L. (2014). Grating-structured freestanding triboelectric-layer nanogenerator for harvesting mechanical energy at 85% total conversion efficiency. Adv. Mater. *26*, 6599–6607, https://doi.org/10.1002/adma.201402428.

Xiong, J., Luo, H., Gao, D., Zhou, X., Cui, P., Thangavel, G., Parida, K., and Lee, P.S. (2019). Self-restoring, waterproof, tunable microstructural shape memory triboelectric nanogenerator for self-powered water temperature sensor. Nano Energy *61*, 584–593, https://doi.org/10.1016/j.nanoen.2019.04.089.

Xu, G., Li, X., Xia, X., Fu, J., Ding, W., and Zi, Y. (2019). On the force and energy conversion in triboelectric nanogenerators. Nano Energy *59*, 154–161, https://doi.org/10.1016/j.nanoen.2019.02.035.

Yan, K., Li, X., Wang, X.X., Yu, M., Fan, Z., Ramakrishna, S., Hu, H., Long, Y.Z., Wang, X.X., and Long, Y.Z. (2020). A non-toxic triboelectric nanogenerator for baby care applications. J. Mater. Chem. A *8*, 22745–22753, https://doi.org/10.1039/d0ta08909e.

Ye, Q., Wu, Y., Qi, Y., Shi, L., Huang, S., Zhang, L., Li, M., Li, W., Zeng, X., Wo, H., et al. (2019). Effects of liquid metal particles on performance of triboelectric nanogenerator with electrospun polyacrylonitrile fiber films. Nano Energy *61*, 381–388, https://doi.org/10.1016/j.nanoen.2019.04.075.

Zhang, C., Tang, W., Han, C., Fan, F., and Wang, Z.L. (2014). Theoretical comparison, equivalent transformation, and conjunction operations of electromagnetic induction generator and triboelectric nanogenerator for harvesting mechanical energy. Adv. Mater. *26*, 3580–3591, https://doi.org/10.1002/adma.201400207.

Zhang, J.H., Li, Y., Du, J., Hao, X., and Wang, Q. (2019a). Bio-inspired hydrophobic/cancellous/hydrophilic Trimurti PVDF mat-based wearable triboelectric nanogenerator designed by self-assembly of electro-pore-creating. Nano Energy *61*, 486–495, https://doi.org/10.1016/j.nanoen.2019.04.065.

Zhang, M., Xia, L., Dang, S., Shi, L., Cao, A., Deng, Q., and Du, C. (2019b). A flexible single-electrode-based triboelectric nanogenerator based on double-sided nanostructures. AIP Adv. *9*, 381–388, https://doi.org/10.1063/1.5114884.

Zhao, J., Zhen, G., Liu, G., Bu, T., Liu, W., Fu, X., Zhang, P., Zhang, C., and Wang, Z.L. (2019). Remarkable merits of triboelectric nanogenerator than electromagnetic generator for harvesting small-amplitude mechanical energy. Nano Energy *61*, 111–118, https://doi.org/10.1016/j.nanoen.2019.04.047.

Zheng, R., Chen, Y., Chi, H., Qiu, H., Xue, H., and Bai, H. (2020). 3D printing of a polydimethylsiloxane/polytetrafluoroethylene composite elastomer and its application in a triboelectric nanogenerator. ACS Appl. Mater. Interfaces *12*, 57441–57449, https://doi.org/10.1021/acsami.0c18201.

Zi, Y., Guo, H., Wen, Z., Yeh, M.H., Hu, C., and Wang, Z.L. (2016). Harvesting low-frequency (<5 Hz) Irregular mechanical energy: a possible killer application of triboelectric nanogenerator. ACS Nano *10*, 4797–4805, https://doi.org/10.1021/acsnano.6b01569.

iScience, Volume *24*

Supplemental information

Comparison of applied torque and energy conversion efficiency between rotational triboelectric nanogenerator and electromagnetic generator

Shaohang Xu, Xianpeng Fu, Guoxu Liu, Tong Tong, Tianzhao Bu, Zhong Lin Wang, and Chi Zhang

Supplemental Figures and Legends

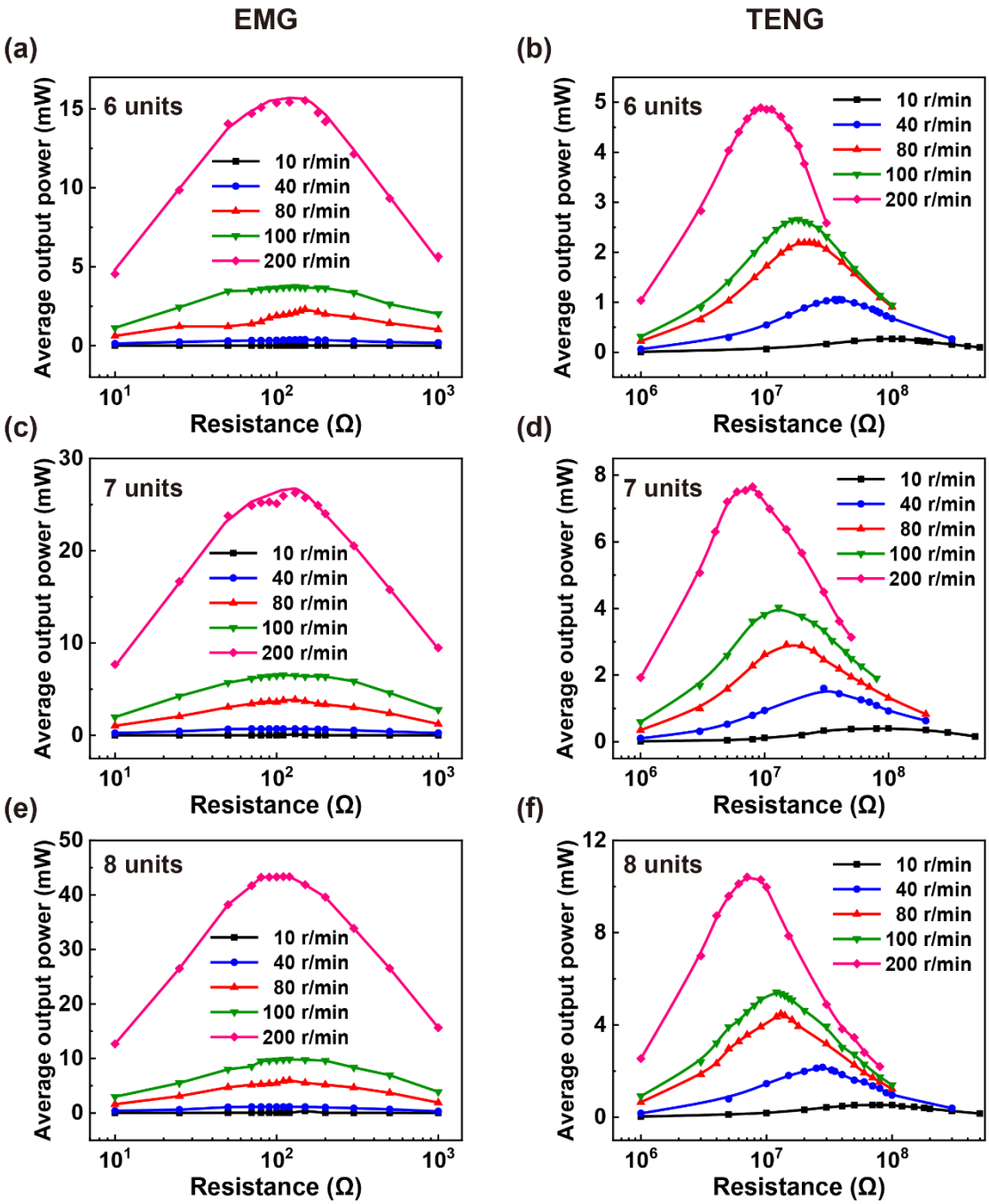

Figure S1. related to Figure 2. Impedance matchings of both generators with different number of power generation units. (a) and (b) 6 units, (c) and (d) 7 units, (e) and (f) 8 units.

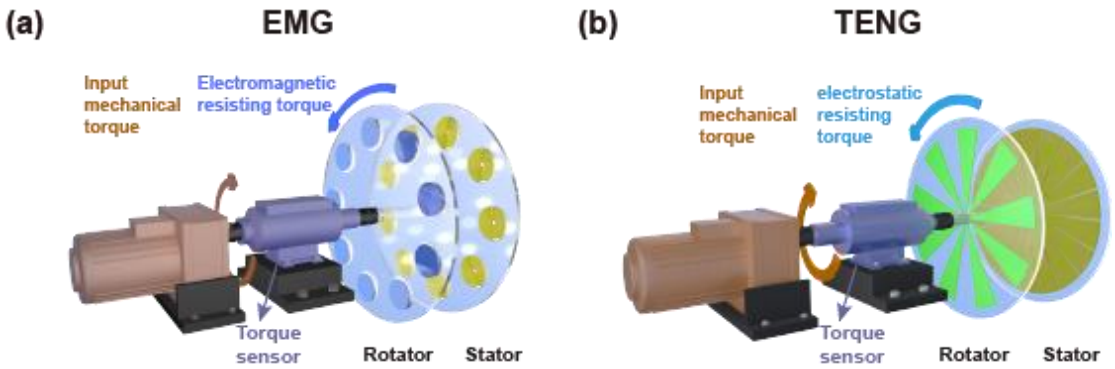

Figure S2. related to Figure 3. The measurement system of both generators. (a) EMG and (b) TENG.

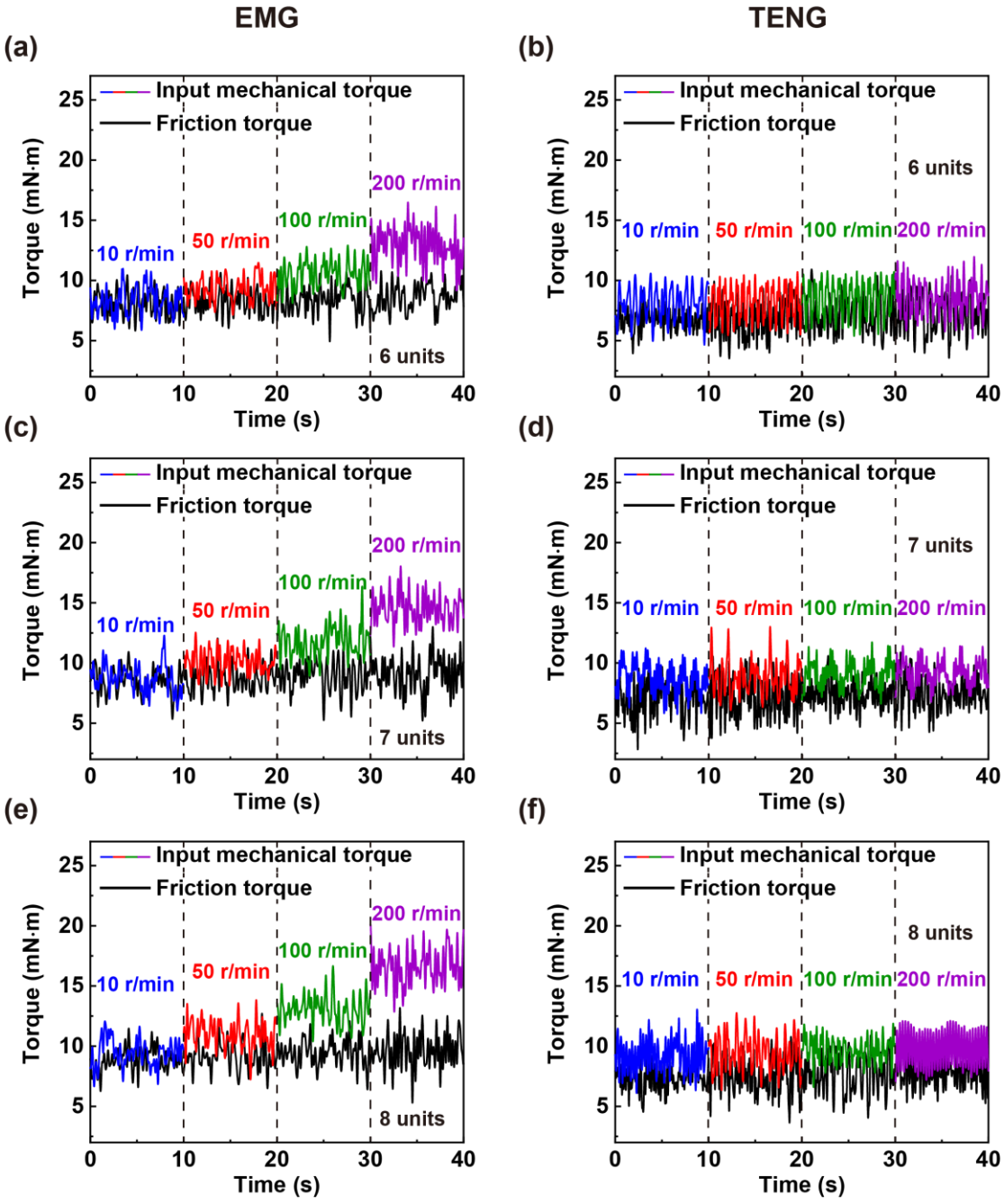

Figure S3. related to Figure 3. The measured torque of both generators with different number of power generation units. (a) and (b) 6 units, (c) and (d) 7 units, (e) and (f) 8 units.

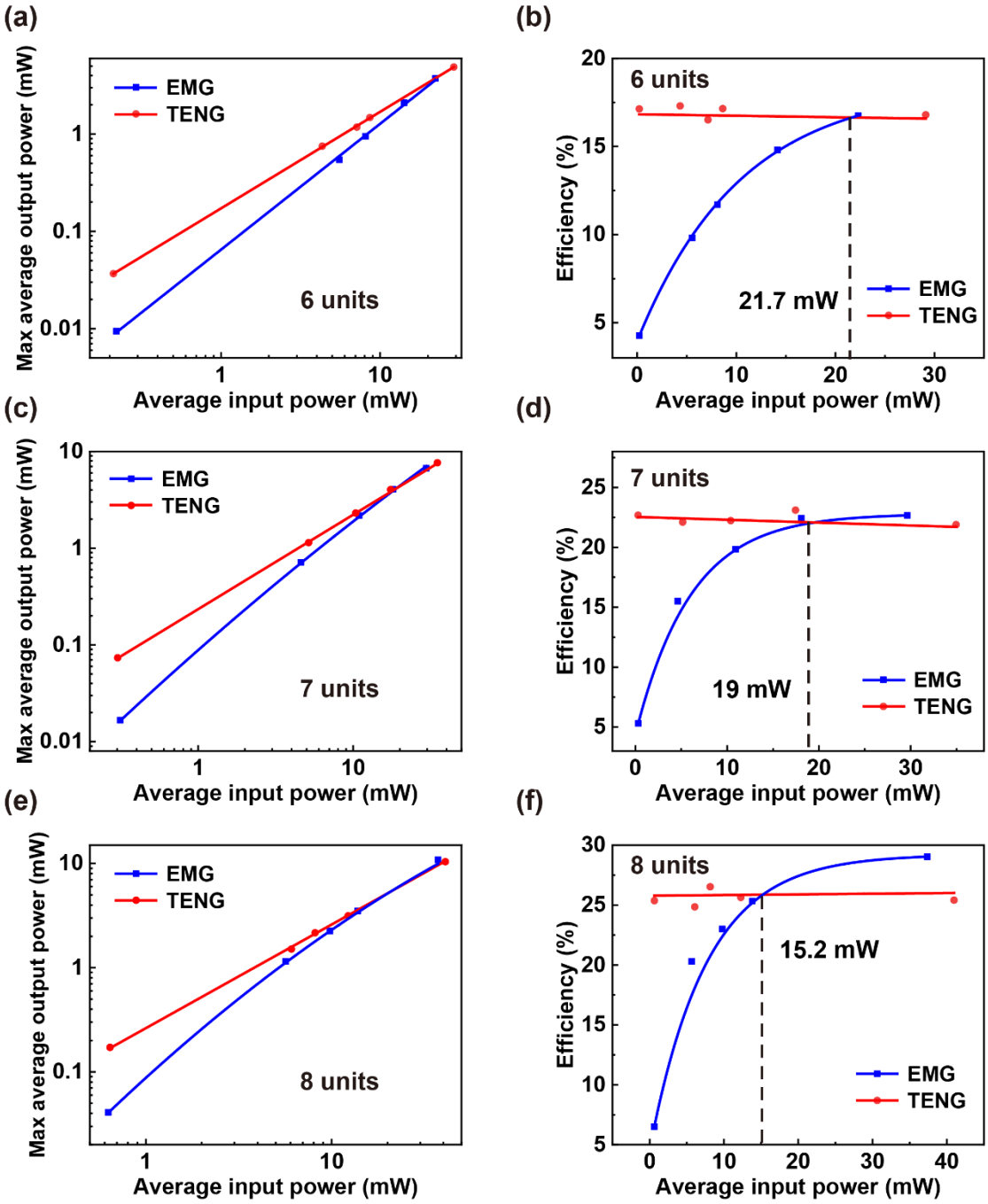

Figure S4. related to Figure 4. Max average output power and energy conversion efficiency comparison of EMG and TENG with different average input power. (a) and (b) 6 units, (c) and (d) 7 units, (e) and (f) 8 units.

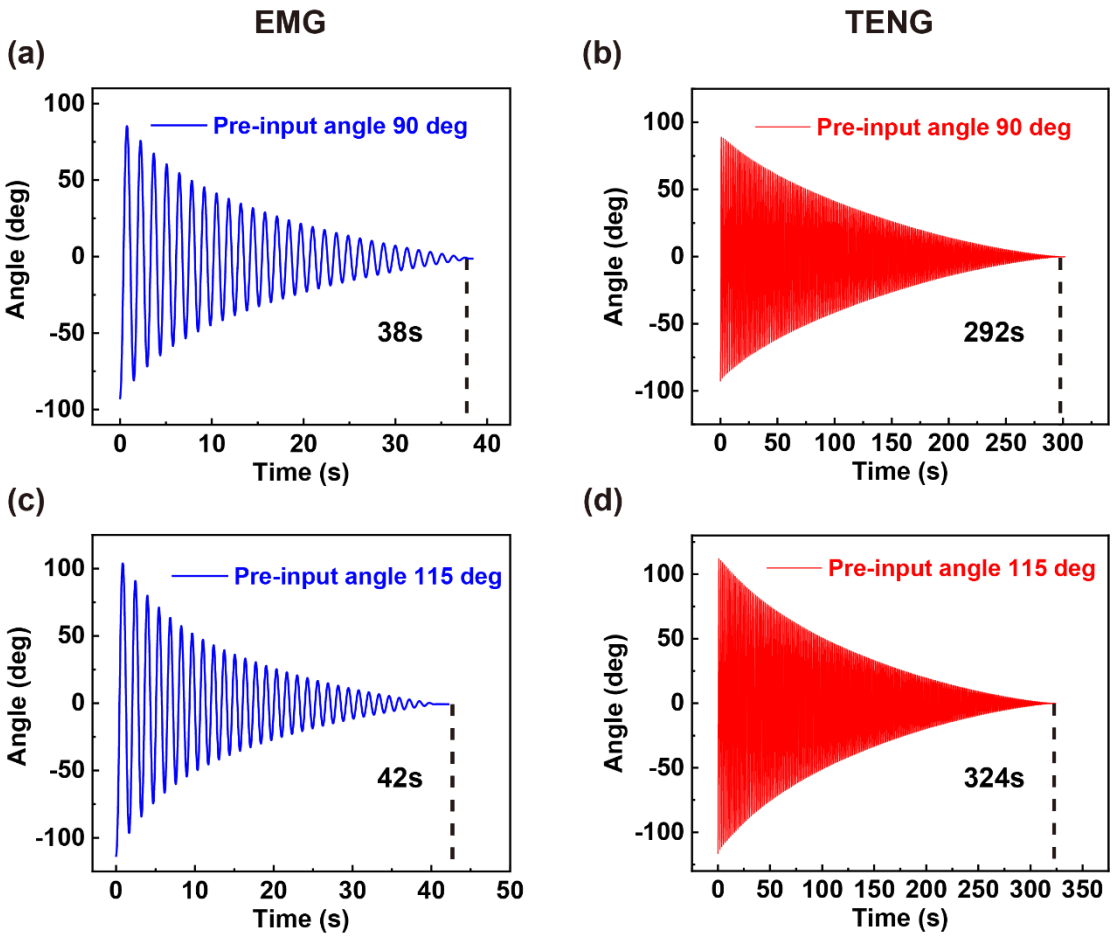

Figure S5. related to Figure 5. The variety of swing angle of EMG and TENG. EMG (a) and TENG (b) at pre-input angle of 90 deg. EMG (c) and TENG (d) at pre-input angle of 115 deg.

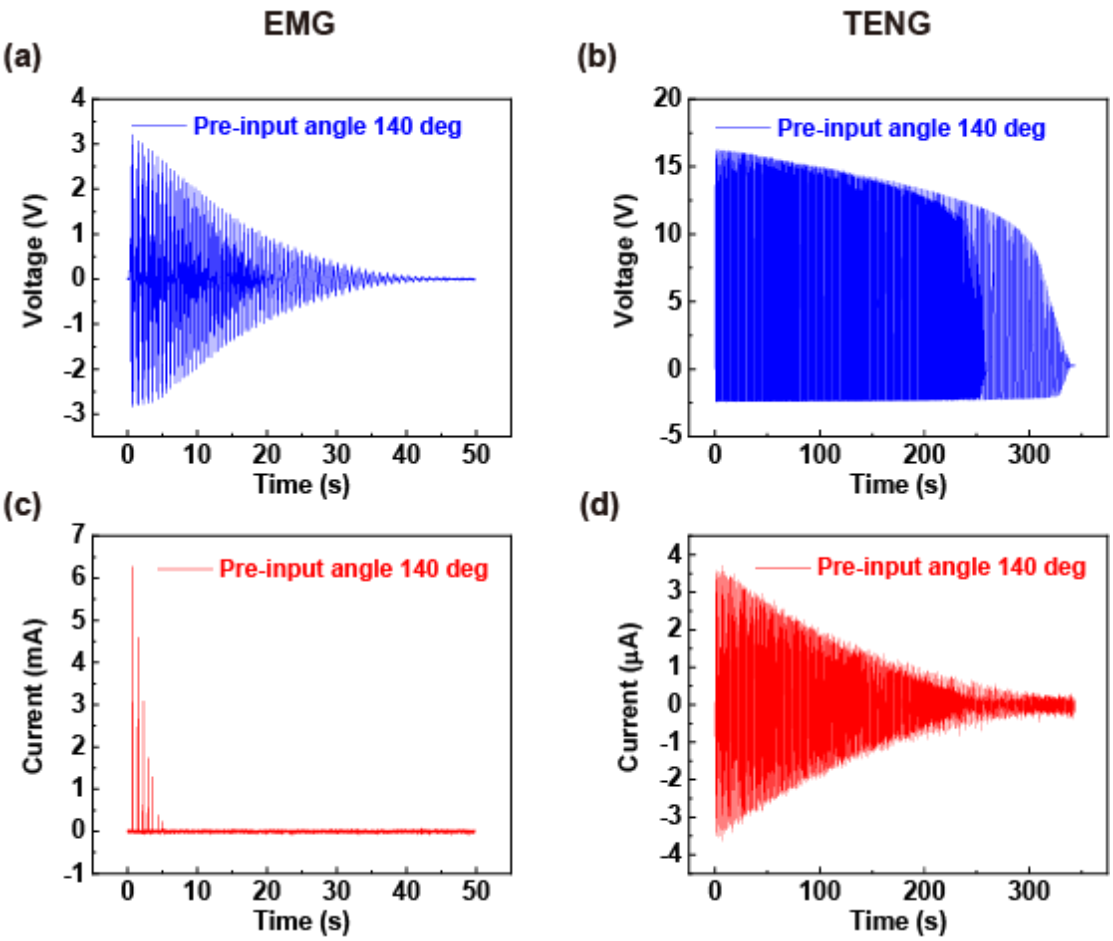

Figure S6. related to Figure 5. Voltage and current across the LED applied by the EMG and TENG at pre-input angle 140 deg. Voltage of the (a) EMG and (b) TENG. Current of the (c) EMG and (d) TENG.

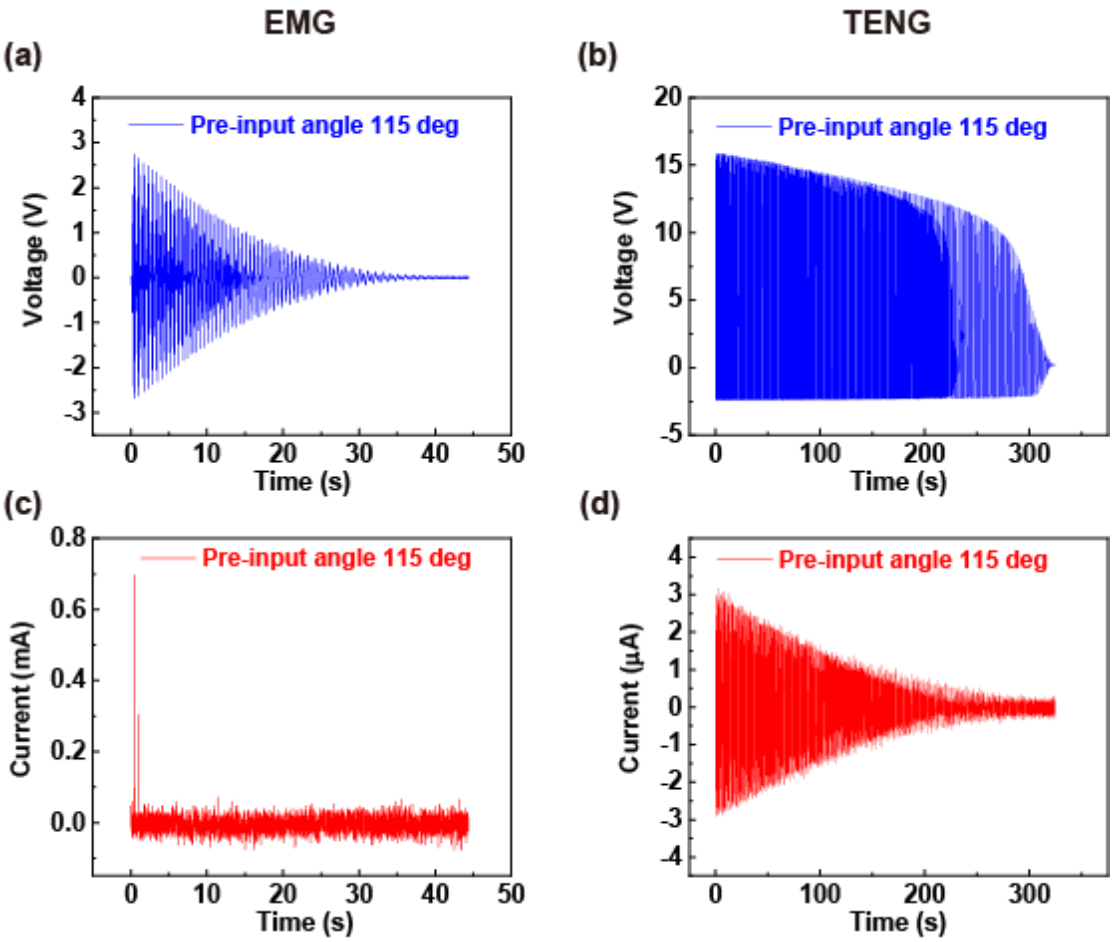

Figure S7. related to Figure 5. Voltage and current across the LED applied by the EMG and TENG at pre-input angle 115 deg. Voltage of the (a) EMG and (b) TENG. Current of the (c) EMG and (d) TENG.

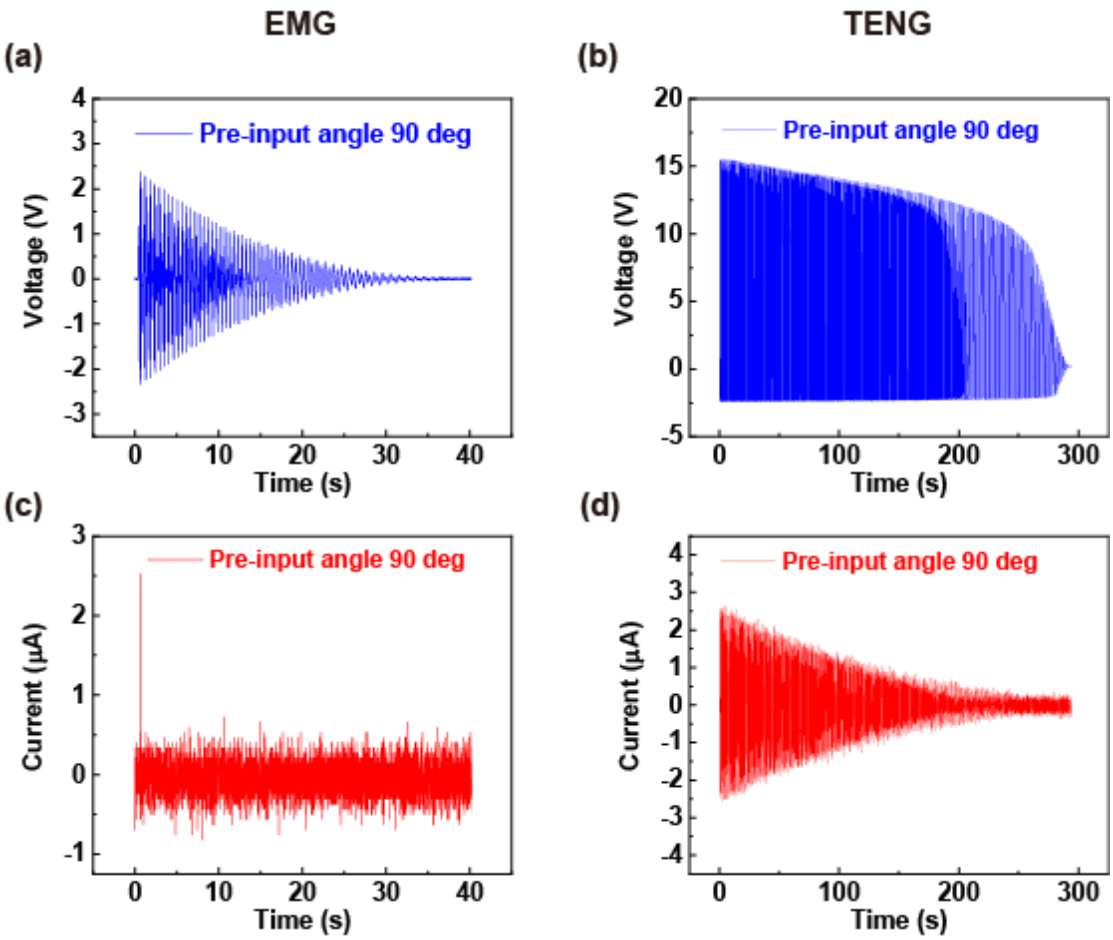

Figure S8. related to Figure 5. Voltage and current across the LED applied by the EMG and TENG at pre-input angle 90 deg. Voltage of the (a) EMG and (b) TENG. Current of the (c) EMG and (d) TENG.

Transparent Methods

Experimental Section

Fabrication of the EMG

First, two nummular acrylics with a diameter of 280 mm are used as the rotator layer and stator layer respectively. Then, the magnets and copper coils are evenly embedded on two nummular acrylics. The magnet is NdFeB with a diameter of 30mm and a height of 5mm. The copper coil also with a diameter of 30mm and a height of 5mm which is formed by winding 3100 loops of enameled wire with a diameter of 0.1mm.

Fabrication of the TENG

First, two nummular acrylics with a diameter of 280 mm are used as the rotator layer and stator layer respectively. Then, the rotator layer of TENG was a nummular acrylic sheet with a diameter of 280 mm, the polarized fluorinated ethylene propylene (FEP) fan-shaped thin films as a triboelectric layer was evenly stuck to one side of the nummular acrylic sheet, the TENG stator layer was a prepared commercialized printed circuit board (PCB) with complementary radially arrayed copper film sectors as another triboelectric layer and the electrodes for electrostatic induction, the PCB was stuck to one side of the another nummular acrylic sheet with a diameter of 280 mm.

Electric measurements

The electrometer (Keithley 6514 system electrometer and Keithley 347 system electrometer) was used to measure the output voltages and currents of both generators. And the angle sensor (BWT61CL) is used to measured swing angle and angular velocity. And the torque sensor (HCNJ-103) is used quantitatively investigates their input mechanical torque of both generators. Meanwhile, a software platform developed based on LabVIEW was used to record the real-time data.